JOURNAL OF ENVIRONMENTAL SCIENCES 156 (2025) 102–113

Available online at www.sciencedirect.com

ScienceDirect

www.elsevier.com/locate/jes

JES JOURNAL OF ENVIRONMENTAL SCIENCES

www.jesc.ac.cn

Research Article

Evolution of global O_3-NO_x-VOCs sensitivity before and after the COVID-19 from the ratio of formaldehyde to NO_2 from satellite observations

Dakang Wang[1,2], *Dongchuan Pu*[3,4], *Isabelle De Smedt*[5], *Lei Zhu*[4,6,7,*], *Xiankun Yang*[1,2,*], *Wenfu Sun*[5], *Hui Xia*[1,2], *Zhaolong Song*[1,2], *Xicheng Li*[4], *Juan Li*[3,4], *Aoxing Zhang*[4,6,7], *Xu Feng*[8], *Yuyang Chen*[4], *Xin Yang*[4,6,7], *Tzung-May Fu*[4,6,7], *Jinnian Wang*[1,2]

[1] *School of Geography and Remote Sensing, Guangzhou University, Guangzhou 510006, China*
[2] *Institute of Aerospace Remote Sensing Innovations, Guangzhou University, Guangzhou 510006, China*
[3] *School of Environment, Harbin Institute of Technology, Harbin 150090, China*
[4] *School of Environmental Science and Engineering, Southern University of Science and Technology, Shenzhen 518055, China*
[5] *Division of Atmospheric Composition, Royal Belgian Institute for Space Aeronomy (BIRA-IASB), Brussels 1180, Belgium*
[6] *Shenzhen Key Laboratory of Precision Measurement and Early Warning Technology for Urban Environmental Health Risks, School of Environmental Science and Engineering, Southern University of Science and Technology, Shenzhen 518055, China*
[7] *Guangdong Provincial Observation and Research Station for Coastal Atmosphere and Climate of the Greater Bay Area, Shenzhen 518055, China*
[8] *John A. Paulson School of Engineering and Applied Sciences, Harvard University, Cambridge 02138, United States*

ARTICLE INFO

Article history:
Received 15 May 2024
Revised 27 July 2024
Accepted 29 July 2024
Available online 5 August 2024

Keywords:
Ozone sensitivity
Satellite formaldehyde (HCHO) and NO_2
Formaldehyde-to-NO_2 ratio
Gross domestic product (GDP)

ABSTRACT

Ozone production sensitivity is widely used to reveal the chemical dominant precursors of urban ozone rise. Here, we diagnose the impact of the decline in global human production activities level caused by the COVID-19 on ozone sensitivity through the ratio of formaldehyde (HCHO) and NO_2 (FNR = HCHO/NO_2) observations from the TROPOspheric Monitoring Instrument. We use a relative uncertainty threshold to clean the satellite FNR, and our satellite FNR present a good correlation ($R = 0.6248$) with U.S. Environmental Protection Agency observations. We found that the outbreak of the COVID-19 did not change the pattern of global ozone sensitivity, while the global regimes was transforming or strengthening to VOC-limited regimes due to the significant decline of human production activities levels. During the COVID-19, ozone sensitivity in Eastern China and East Africa continued to shift to VOC-limited regimes, while India, Western Europe and North America first moved to NO_x-limited regimes, and then changed to VOC-limited regimes with the resumption of

* Corresponding authors.
E-mails: zhul3@sustech.edu.cn (L. Zhu), yangxk@gzhu.edu.cn (X. Yang).

https://doi.org/10.1016/j.jes.2024.07.029

production and the increase in travel. The clustering results tell that urban ozone sensitivity tends to shift towards NO_x-limited regimes as economic growing. The ozone formation in cities with lower FNR and per capita gross domestic product (GDP) are more sensitive to changes in VOCs, while cities with higher FNR and per capita GDP are more sensitive to variations in NO_x. Cities with intermediate FNR and GDP are good evidence of the existence of transitional regimes. Our study identifies the driving role of urban economics in orienting the evolution of ozone sensitivity regimes.

Introduction

Volatile organic compounds (VOCs) and nitrogen oxides (NO_x) are the precursors for ozone formation (Wang et al., 2022). Since Seinfeld (1989) announced that the ratio of VOCs to NO_x could be used for indicating the photochemical regime of ozone formation, as one proxy for VOCs/NO_x, the ratio of formaldehyde to NO_2 (FNR = HCHO/NO_2) (Sillman and Samson, 1995) has been widely analyzed for figuring out the O_3–NO_x–VOC photochemistry sensitivity, from a laboratory (Jeon et al., 2018; Liu et al., 2021) or space perspective (Jin et al., 2020; Lee et al., 2022; Li et al., 2021a; Ren et al., 2022a; Schroeder et al., 2017; Xue et al., 2022). Multiple evaluative studies have demonstrated the reliability of FNR as an indicator of ozone sensitivity (Hong et al., 2021; Liu et al., 2021; Souri et al., 2020).

With the emergence of more research on FNR, it seems that there is no specific FNR threshold that could generalize the global ozone formation control regime, which is determined by the differences in atmospheric environment, surface heterogeneity, and ozone emissions in local regions(Campbell et al., 2015; Dunker et al., 2020; Jin et al., 2017; Ren et al., 2022b). But we can roughly determine the orientation of dominant factor in O_3–NO_x–VOC sensitivity through the increasing or decreasing trend of FNR (Liu and Shi, 2021; Ren et al., 2022b; Vazquez Santiago et al., 2024), thus providing local governments with strategies to mitigate ozone pollution.

The COVID-19 pandemic lasted for nearly three years (December 2019 to December 2022). During this period, almost all countries took measures to reduce human activities, including lock down city, control crowd gathering, transportation, and industrial production to prevent the rapid spread of the virus. The drastic reduction in human activities worldwide has led to significant changes in the emissions of atmospheric pollutants and their precursors (Facciolà et al., 2021). Recent studies have noted the changes in anthropogenic emissions of non-methane Volatile organic compound (HCHO as the proxy) (Sun et al., 2021a; Yen et al., 2023), nitrogen oxides (NO_x) emissions (NO_2 as the proxy) (Bauwens et al., 2020; Cooper et al., 2022; Kerr et al., 2021; Li et al., 2021b; Misra et al., 2021) and ozone pollution (Campbell et al., 2021; Miyazaki et al., 2020) during the outbreak of the COVID-19 pandemic, while the changes in the sensitivity of global O_3–NO_x–VOC caused by the COVID-19 pandemic remains unclear.

The development of the economy produces driving effect on the emissions of HCHO (Dienhart et al., 2021; Huang et al., 2023; Sun et al., 2021b), NO_2 (Jones et al., 2023; Savtchenko and Khayat, 2021; Stavrakou et al., 2020), and O_3 (Selin et al., 2009; Stowell et al., 2017; Zhan et al., 2023). The relationship between rapid economic growth and ozone precursors on a global scale is not clear (Verstraeten et al., 2015) and depends on government decision-making guidance. Practical cases in more developed cities can provide us with valuable references. The COVID-19 has brought unforgettable pain to people around the world, but it has also provided an opportunity to do research on the impact of changes in human activity and economic development on the atmospheric environment on a global scale, such as O_3–NO_x–VOC sensitivity. This study calculates the global tropospheric FNR using the vertical column concentrations of HCHO and NO_2 observed by satellite through a strict threshold control method, establishes the relationship between O_3–NO_x–VOC sensitivity and the indicator factor of the economic development level of global metropolises, and clarifies the driving direction of the global human activity reduction caused by the COVID-19 epidemic to O_3–NO_x–VOC sensitivity. FNR has been used to indicate the O_3–NO_x–VOC sensitivity for a long time, but there is still no unified FNR threshold to figure out the dominant factor of O_3 sensitivity regimes, although FNR indicator ratio is well-suited for satellite data analyses (Jin et al., 2020; Jin and Holloway, 2015; Johnson et al., 2023; Martin et al., 2004; Schroeder et al., 2017), Acdan et al. (2023) comprehensively discussed the limitations of TROPOMI FNR from four aspects and suggested that changes in O_3 chemistry sensitivity between composite categories should be best viewed through a qualitative lens. This paper determines the evolutionary orientation of O_3 sensitivity regimes in major developed regions and megacities around the world according to the trend of FNR, in order to discover how developed megacities around the world should mitigate O_3 pollution by adjusting VOC and NO_x emissions.

1. Materials and methods

1.1. *EPA surface observations of air quality*

We obtain surface HCHO and NO_2 observations from the U.S. Environmental Protection Agency (EPA) operated by states, local agencies, and tribes (SLTs network), available at https://www.epa.gov/outdoor-air-quality-data. EPA SLTs sites report 24 h average HCHO concentrations every 6 days and hourly

Table 1 – Number of sites in pretreatment

Year	HCHO	NO_2	HCHO ∩ NO_2	Ground FNR ∩ Satellite FNR
2019	109	455	55	37
2020	102	453	51	35
2021	106	462	55	38

NO_2 concentration observations on a daily basis. We plan to compare the FNR from satellite (a local cross-time of 13:30) with the ratio of surface HCHO concentration to NO_2 concentration (EPA FNR) at midday. Due to the lack of hourly surface HCHO observations, we managed to convert the daily average into midday concentration. Zhu et al. (2017) successfully used high-quality ground-site HCHO measurements to convert midday to 24 h averaged surface summer air HCHO concentrations, a comprehensive scaling factor $\gamma_2 = 0.73$ was applied throughout the whole U.S. The γ_2 was used in this paper to obtain the surface formaldehyde concentration at midday from Eq. (1). Due to the dry deposition of formaldehyde at night, although the 24 h average to midday value ratio is consistent at several stations in Zhu et al. (2017), geographical specificity have a non-negligible impact on this ratio. More consideration of surface anisotropy in γ_2 will be able to further improve the accuracy of the conversion, which may require more ground-based observations to support this work. The surface NO_2 concentration at midday was derived from the average of observations at 13:00 and 14:00 local time. We obtained full year HCHO and NO_2 concentration data for 2019-2021 from the EPA SLTs network, after tedious preprocessing, the number of sites is summarized in Table 1. The second and third columns represent the number of all sites for HCHO and NO_2 collected from EPA SLTs network, the fourth column represents the number of sites with both daily HCHO and NO_2 observations, and the fifth column represents the reserved sites whose positions correspond to satellite pixels that captured FNR at local cross-time of satellite. 24-hour observation and WGS84 coordinate system were used as additional screening criteria during the processing. Locations of the sites that meets the fifth column condition is shown in Fig. 1, which will be used to verify the satellite FNR.

$$C_{midday}^{HCHO}(n) = \frac{C_{daily}^{HCHO}(n)}{\gamma_2} \quad (1)$$

where, $C_{midday}^{HCHO}(n)$ (ppb) and $C_{daily}^{HCHO}(n)$ (ppb) are the surface formaldehyde concentration of midday and 24 h average from the site n, respectively; γ_2 is the ratio of 24 h averaged surface HCHO concentrations to midday, with value of 0.73.

1.2. *Satellite observations of air quality*

TROPOMI is a nadir-viewing hyperspectral spectrometer on board the Copernicus Sentinel-5 Precursor platform launched in October 2017, which observes the whole globe daily at 13:30 local time. Daily offline level 2 TROPOMI tropospheric HCHO and NO_2 vertical columns density (VCD) has been published on NASA official website (https://disc.gsfc.nasa.gov/) with a much fine nadir spatial resolution of 7.0 × 3.5 km^2 (upgraded to 5.5 × 3.5 km^2 since August 2019) and signal-to-noise ratio, retrieved from ultraviolet spectral measurements with the method of Differential Optical Absorption Spectroscopy (DOAS). TROPOMI HCHO (de Smedt et al., 2021) and NO_2 VCD (van Geffen et al., 2022) have been conducted consolidated ground-based validation against observations from the Multi-AXis Differential Optical Absorption Spectroscopy (MAX-DOAS) (Chan et al., 2020), Fourier-transform infrared (FTIR) (Vigouroux et al., 2020), Network for the Detection of Atmospheric Composition Change (NDACC) and direct sun (DS) observations from Pandonia Global Network (PGN) (Verhoelst et al., 2021). HCHO columns show mean bias ranging from −26.0 % to +30.8 %, and NO_2 columns show a negative bias of typically −23 % to −50 %, depending on the degree of contamination in the area.

TROPOMI HCHO and NO_2 columns from December 1, 2018 to December 31, 2021 was used for examining changes in satellite FNR before and after the outbreak of the COVID-19 (with December 2018 to December 2019 for the period before the outbreak of the COVID-19, December 2019 to December 2020 for the peak period of the COVID-19 and December 2020 to December 2021 for the period of COVID-19 relief). As a primary selection for the data, quality assurance value greater than 0.5, cloud fraction less than 0.3, and solar zenith angle less than 60° are set to retain high-quality raw data, further data control will be conducted in FNR. The FNR of Level 2 is worked out at the pixel level, and the FNR is recorded only if both HCHO and NO_2 have values at the same pixel, otherwise it will be null. We then regrid all level-2 FNR onto the 0.05° × 0.05° (~5 × 5 km^2) grids using our regridding method and filter these grids with a relative uncertainty of 0.2, which is determined by a complicated uncertainty propagation formula.

1.3. *Gross domestic product*

The Gross domestic product (GDP) per Capita data of major cities in the world of 2020 in this study comes from public data released by the World Bank (https://dataworldbank.org), which is widely cited (Wang and Li, 2021). We compiled the data and ranked the top 100 cities, and assumed that the rankings are unchanged for 2019 and 2021. Given the impact of the global blockade caused by the COVID-19 on the HCHO (Sun et al., 2021a) and NO_2 (Cooper et al., 2022) patterns, this research aims to explore how the large-scale decline of human production activities caused by the COVID-19 affects the ozone sensitivity (indicated by FNR). Comprehensive factor GDP is selected to examine the relationship between economic development and FNR under the influence of the COVID-19, and excavate the evolution of FNR at various levels of economic development.

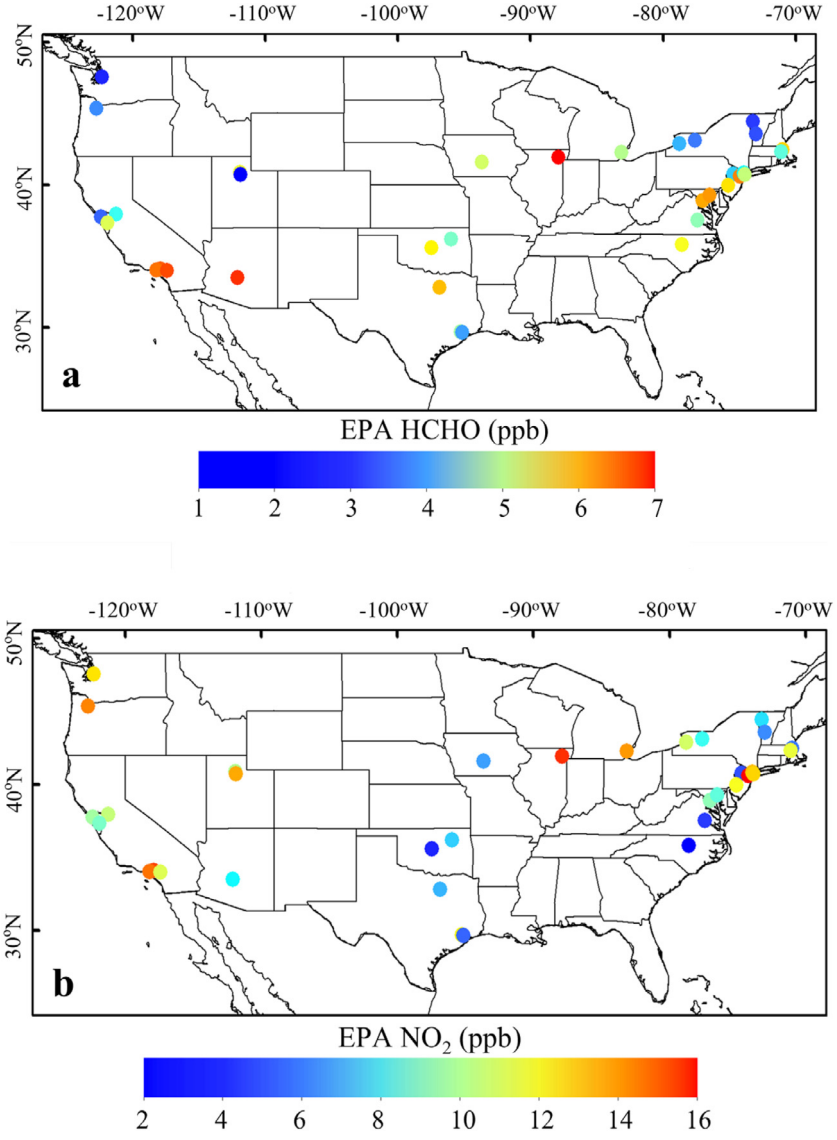

Fig. 1 – (a) Annual mean 2019-2021 HCHO and (b) NO_2 concentrations from the EPA surface network (SLTs) and the network site locations

1.4. *Regridding and propagation of uncertainty*

Our regridding algorithm achieves grid data with higher spatial resolution and higher signal-to-noise ratio by stacking multi-phase satellite observations (Sun et al., 2018; Zhu et al., 2014). The principle can be illustrated by a common case that overlapping between pixels and grids. As shown in Fig. 2, consider that a grid overlaps with multiple pixels (p), and the area ratio of each overlapping part to the original pixel is $w_p = \frac{O(p,i)}{S(p)}$. The FNR of grid i will be figured out from Eq. (2).

$$FNR(i) = \frac{\sum_{p=1}^{P(i)} \frac{O(p,i)}{S(p)\sigma(p)} |FNR(p)|}{\sum_{1}^{p(i)} \frac{O(p,i)}{S(p)\sigma(p)}} \quad (2)$$

where, $O(p,i)$ (km^2) is the overlap area between the pixel p and grid i, $S(p)$ (km^2) is the p_{th} pixel area which overlaps the grid i, $\sigma(p)$ (molecules/cm^2) is the absolute error standard deviation

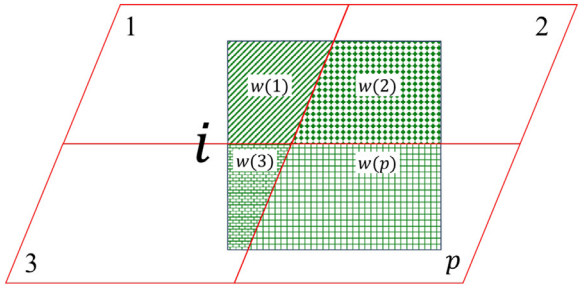

Fig. 2 – Schematic diagram of regridding

of the p_{th} pixel, read from the product field, $|FNR(p)|$ is the FNR of the p_{th} pixel, represented as $\frac{\Omega(p)_{HCHO}}{\Omega(p)_{NO_2}}$.

Functionalization of raw data will trigger the propagation of uncertainty (Crowder et al., 2020; Larson, 1986). The ini-

tial uncertainty of each pixel and the contribution weight of which to the grid finally produce the new uncertainty for resampled grid. Quantifying uncertainty is an effective diagnosis of computational results and helps with strict data quality control. van Geffen et al. (2022a) reported a total relative uncertainty of 15 %-50 % for TROPOMI NO_2 VCD for larger columns over continental areas, while de Smedt et al. (2021) disclosed the total uncertainty in HCHO tropospheric VCD retrievals is estimated to be between 30 %–60 % in polluted conditions. Souri et al. (2023) published that the satellite column retrieval error is the largest contributor to the total error (40 %–90 %) in the FNR using an equation that propagating individual uncertainty in their paper, without depicting the propagation of uncertainty during regridding. Our Eq. (3) works out the propagation of uncertainty in calculating ratio and regridding. Assuming that the pixels crossing the same grid on the Sentinel-5P satellite image are independent of each other, and that the HCHO and NO_2 columns at the same pixel are also independent of each other (i.e., the correlation coefficient is 0), we tracked the propagation of uncertainty (PU) generated during the process of calculating FNR from HCHO and NO_2 and regrid it, as shown in Eq. (3).

$$\sigma_{FNR\_Oversampling} = \sqrt{\frac{\sum_{p=1}^{P(i)}\left[\frac{O(p,i)}{S(p)}\cdot\left[|FNR(p)|\cdot\sqrt{\left(\frac{\sigma(p)_{HCHO}}{\Omega(p)_{HCHO}}\right)^2+\left(\frac{\sigma(p)_{NO_2}}{\Omega(p)_{NO_2}}\right)^2}\right]\right]^2}{\left[\sum_{p=1}^{P(i)}\frac{O(p,i)}{S(p)}\right]^2}} \quad (3)$$

where, $\sigma(p)_{HCHO}$ (molecules/cm^2) is the uncertainty of the HCHO column density at the p_{th} pixel, $\sigma(p)_{NO_2}$ (molecules/cm^2) is the uncertainty of the NO_2 column density at the p_{th} pixel, and $\Omega(p)_{HCHO}$ (molecules/cm^2) is the HCHO column density at the p_{th} pixel, $\Omega(p)_{NO_2}$ (molecules/cm^2) is the NO_2 column density at the p_{th} pixel.

2. Results and discussion

2.1. *Comparison between TROPOMI FNR and surface observations*

Due to environmental interference and the limitation of sensor performance, it is not easy to ensure that all EPA HCHO and NO_2 sites have satellite data covered daily. The fifth column of Table 1 gives the number of sites cross with pixel FNR. We further excluded FNR with relative uncertainty greater than 20 % or less than 0 to retain high-quality data. The implementation of relative uncertainty thresholds also reduces the number of mappings between EPA sites and TROPOMI FNR. 768 sets of daily observations were ultimately preserved.

Fig. 3 shows a significant positive correlation between EPA FNR and TROPOMI FNR, with a correlation coefficient of 0.6248. Most of the points are concentrated in the range of EPA FNR less than 1, where the correlation between the two is poor (R is less than 0.36, as shown in Fig. 4). However, in the range of EPA FNR greater than 1, the correlation between the two is better than that case. More samples and high values of FNR resulted

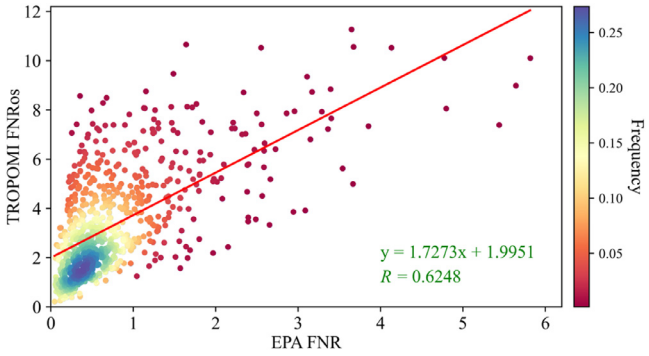

Fig. 3 – Comparison between TROPOMI FNR ($HCHO/NO_2$) and EPA FNR

in an increase in the correlation coefficient between TROPOMI FNR and EPA FNR, which is more conclusive evidence in Fig. 4. Fig. 4 reveals the correlation between TROPOMI FNR and EPA FNR in the case of ERA FNR is less than a certain threshold. The horizontal axis represents the threshold set each time, and the vertical axis indicates the correlation between TROPOMI FNR and EPA FNR under the constraint of this threshold. The pink line indicates the correlation trend when EPA FNR is below the threshold, while the blue line shows the correlation trend when EAP FNR is above the threshold. Whether as the threshold increases or decreases, a conclusion is drawn that an increase in sample size promotes an increase in correlation coefficient. More specifically, we found that when EPA FNR exceeds 2, the addition of high FNR values leads to a decrease in the rate of increase in correlation coefficients.

Fig. 5 shows the comparison of monthly mean between EPA FNR and TROPOMI FNR. It should be noted that not all gridded TROPOMI FNR corresponding to EPA sites were used to calculate monthly average. Here, we show monthly mean EPA FNR and TROPOMI FNR that meet the 6-day interval. We can intuitively note that TROPOMI FNR is significantly higher than EPA FNR at almost all sites, but both show similar evolutionary trends. Although we cannot analyze the temporal evolution of FNR at the same site due to differences in site location, we can also find that lower FNR generally occurs from January to April each year, while higher values typically occur from June to October, depending on the species and degree of pollution. TROPOMI FNR performs a good correlation and a relatively consistent evolution trend with EPA FNR, can serve as an important indicator of surface ozone sensitivity.

2.2. *Global variation in FNR during the COVID-19 pandemic*

We used level 2 daily TROPOMI HCHO VCD and NO_2 VCD to compute FNR at the pixel level and then the daily level 2 FNRs were spatially overlaid and regridded within a year to achieve the global annual mean TROPOMI FNR (Fig. 6a-c). The propagation of uncertainty from the original TROPOMI observations was also quantified, and relative uncertainties greater than 1 were excluded (Fig. 6d-f). The outbreak of the COVID-19 pandemic did not significantly change the global distribution of FNR (Fig. 6a-c), that is, the global O_3–NO_x–VOC sensi-

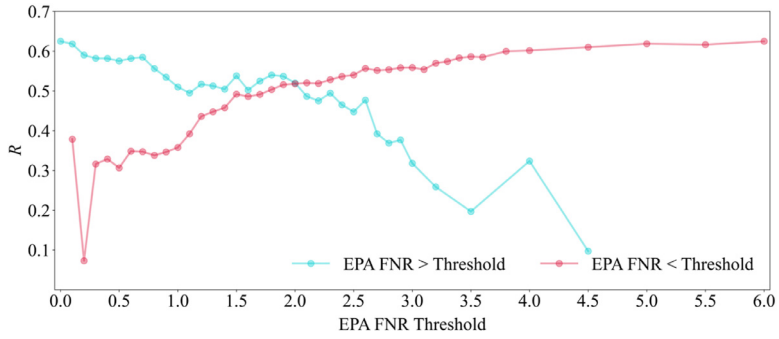

Fig. 4 – Evolution of correlation between TROPOMI FNR ($HCHO/NO_2$) and EPA FNR

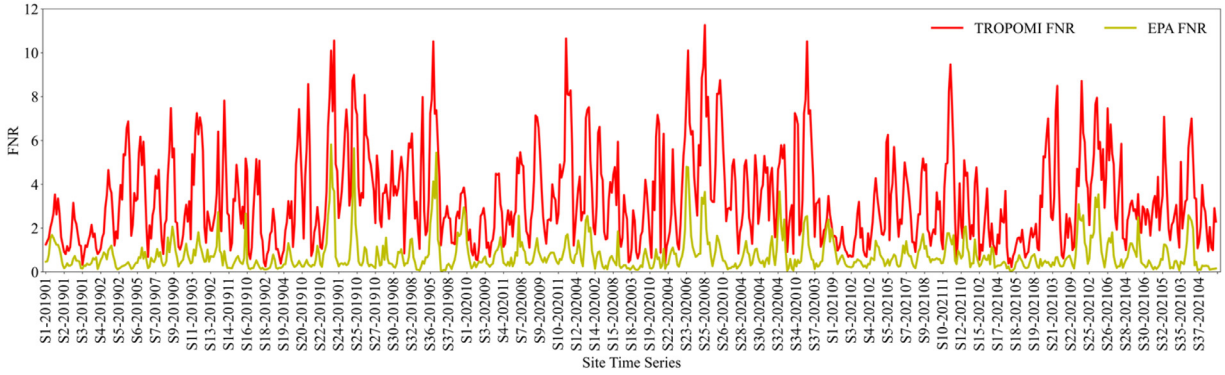

Fig. 5 – Evolution of monthly mean between TROPOMI FNR ($HCHO/NO_2$) and EPA FNR (with S1-201901 refers to the FNR for January 2019 of the site encoded as S1)

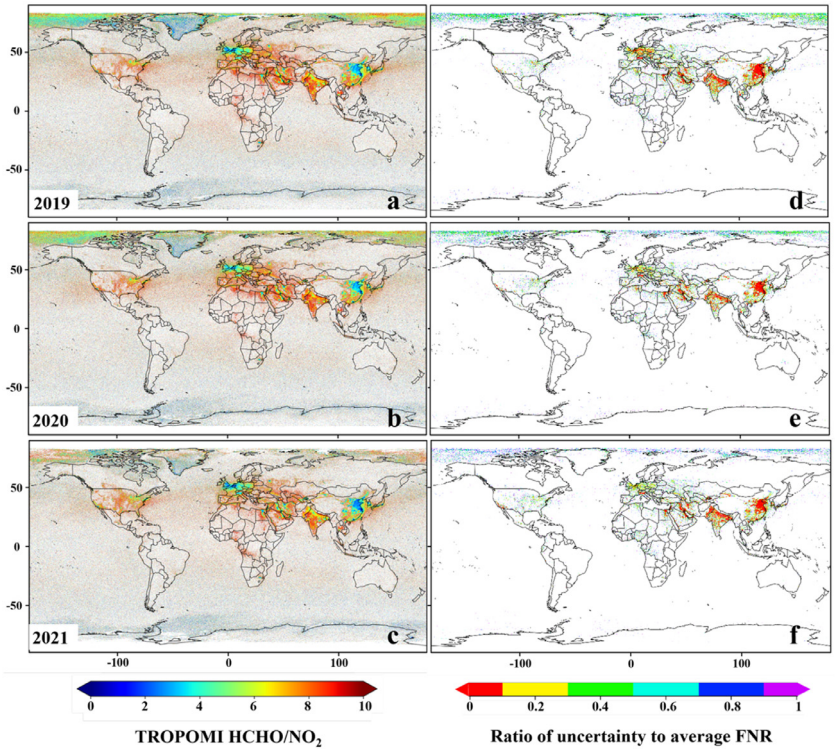

Fig. 6 – (a-c) Annual mean TROPOMI FNR ($HCHO/NO_2$) and (d-f) the relative uncertainty (values greater than 1 have been blanked)

Table 2 – Annual average FNR ($HCHO/NO_2$) of typical regions worldwide

Region	FNR		
	2019	2020	2021
Eastern China	4.48	4.20	3.70
India	7.03	7.30	6.64
East Africa	6.27	6.05	5.40
Western Europe	4.85	4.96	4.04
North America	5.91	6.07	5.27

tivity pattern was not significantly affected. Under the treatment scheme of this research, FNR was more concentrated in eastern China (mainly east of the Hu Line), the whole of India, Eurasia, western Europe, and the central and eastern North America, where the population is concentrated and the economy are relatively developed. FNR is generally small in areas with low population distribution, including typical oceans, deserts (e.g., the Sahara Desert, the Taklamakan Desert in northwestern China), African savannah, South America, Oceania, Canada, and Russia. The FNR with large relative uncertainty (> 100 %) were mainly found in regions with low levels of vegetation and anthropogenic sources, while low uncertainty (50 %) is mainly in areas with concentrated populations and developed economies, which provided strong signals (Fig. 6d-f). Our results are very consistent with those of Souri et al. (2023). Regions with large relative uncertainty would be cleaned by relative uncertainty threshold of 0.2 to do more reliable analysis for urban ozone sensitivity regimes. Since the epidemic, the global FNR has shown a decreasing trend from 2019 to 2021, the global average filtered by the relative uncertainty of 0.2 are 5.67, 5.64, and 5.04, respectively, indicating that on a global scale, ozone formation will evolve towards to be more sensitive to VOCs. Fig. 7 shows the FNR of regions with high levels of human activity around the world, using the threshold method to filter the areas with low levels of human activity to observe spatial changes in FNR due to human influence. The low FNR in eastern China are mainly distributed in several economically developed regions, including the Yangtze River Delta region and the Pearl River Delta region, and India, East Africa and North America have demonstrated the urban agglomeration effect of FNR and ozone. In Western Europe, where the economy is generally more developed, the FNR is lower in the UK and the Netherlands, indicating that the formation of ozone here is more likely sensitive to VOCs, while generally higher in the rest of the area, with opposite ozone sensitivity regimes for the two. Table 2 shows the statistics of FNR in typical areas of each continent, and it can be seen that from 2019 to 2021, both eastern China and East Africa show a continuous decreasing trend, while India, Western Europe and North America have similar conditions, all of which increase first and then decrease, indicating that the ozone sensitivity regimes will gradually change to be VOCs-limited with the development of the economy and the resumption of work and production in areas with high human activity level. It is worth noting that a common feature of these regions is that the FNR in 2021 decreased significantly compared to the previous two years, which may be attributed to the rise in NO_x emissions caused by the gradual increase in the level of human activity in the later of the COVID-19.

The average FNR of the top 100 cities ranked by global GDP from 2019 to 2021 was quantified (Fig. 8a) using TROPOMI observations. Overall, FNR in 2021 is the lowest, FNR in 2020 is the highest for almost all cities. The COVID-19 broke out in December 2019, and then the level of human production and activities declined sharply in 2020. The global COVID-19 in 2020 is the most severe period. Although the global plant closure or production reduction will cause the decline of VOCs emissions, the reduction of NO_x was more obvious due to the reduction of human activities and the implementation of the city closure policy, which is the main reason for the sudden increase of global FNR in 2020. With the gradual suppression of the epidemic and the reduction of people's fear of the epidemic, the resumption of work and production and travel raised in 2021, the increase of NO_x emissions was the reason for the lowest FNR in 2021. It can be found from Fig. 8a that Houston has an abnormally high FNR for three consecutive years, and there is no significant change in FNR over these three years. Such a high FNR indicates that the overall ozone sensitivity in Houston is a NO_x-limited regimes, while Suzhou, Moscow, and Riyadh show abnormally low FNR in 2019-2021, with no significant change. Such a low FNR means that the overall sensitivity of ozone in Moscow is manifested by the VOCs-limited regimes. Stockholm did not conduct statistics here due to its limited data volume. Fig. 8b shows the average FNR of the top 100 cities from 2019 to 2021, with the green represents the average (FNR_noPU) without performing uncertainty propagation, the red represents the average (FNR_PU) filtered by relative uncertainty of 0.2 calculated with uncertainty propagation, and the shaded red shading showing the uncertainty of the three-year average FNR. It can be seen that there is a significant difference in FNR between unthresholded and thresholded in most cities, with the most significant difference observed in Chengdu, Shizuoka, and Indianapolis. From the three-year average FNR, abnormal high FNR of Houston is still the most prominent, while Suzhou, Moscow, and Riyadh still show the lowest FNR. There is no significant difference in the uncertainty of FNR among cities after filtering through the FNR threshold. The threshold method effectively eliminates the noise interference caused by the original satellite columns.

2.3. *Urban ozone sensitivity regimes oriented by economic development*

The K-means algorithm was used to cluster the top 100 cities according to GDP per capita and FNR, resulting in 7 clusters, Houston's particularity made it a separate category (Fig. 9). Along the horizontal axis, the clusters are divided into three echelons, namely the first echelon (Cluster 3 and Cluster 5), the second echelon (Cluster 1, Cluster 4 and Cluster 6) and the third echelon (Cluster 2), the average curve slope for each echelon is $k_{h1} = -3 \times 10^{-6}$, $k_{h2} = 8.3 \times 10^{-6}$, $k_{h3} = 9 \times 10^{-6}$. $k_{h1} < k_{h2} < k_{h3}$, which indicated that with the increase of GDP per capita, FNR had a tendency to rise, and the urban ozone sensitivity regimes developed towards NO_x-limited during the COVID-19 pandemic. Along the vertical axis, the clus-

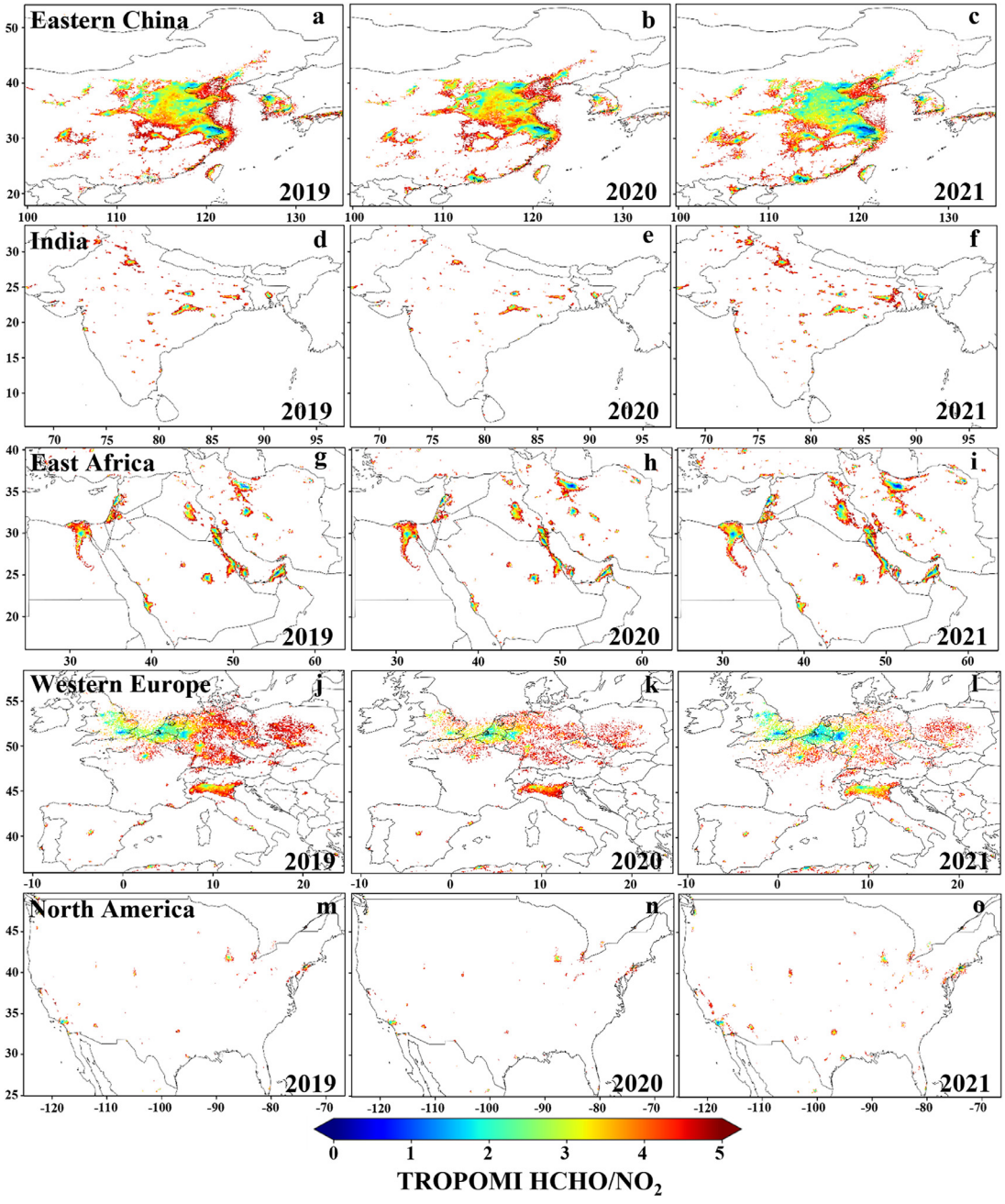

Fig. 7 – FNR ($HCHO/NO_2$) in areas with high human activity across continents

ters are also divided into three echelons, namely the first echelon (Cluster 3 and Cluster 1), the second echelon (Cluster 5, Cluster 4 and Cluster 2) and the third echelon (Cluster 6). Vertically, there are significant differences in FNR among cities with similar GDP per capita, while horizontally, there are gaps in the level of economic development between cities with similar FNR levels, indicating that ozone sensitivity would change at different stages of economic development, and also proving the existence of transition regimes.

Line 8 is the fitting curve between FNR and per capita GDP of cities in Clusters 1, 2 and 3, and there is a good correlation between FNR and per capita GDP ($R = 0.78$, $k8 > 0$), and $k3 < k1 < k2$, which shows an upward trend, implying that the evolution trajectory of international urban ozone sensitivity is that FNR show an raising trend with the increase of economic level, urban O_3 sensitivity regimes gradually evolve from VOC-limited to NO_x-limited regimes, and O_3 formation become more and more dependent on NO_x-limited regimes, the economic level has gradually become a positive driving force for the rise of FNR, and the improvement of economic level promotes the evolution of ozone sensitivity towards NO_x regimes. Line 9 is the fitting curve of per capita GDP and FNR for cities in clusters 5, 4 and 2. In the regions with higher FNR, cities with different economic levels have similar O_3 sensitivity regimes. FNR showed an upward trend with the development of the economy, suggesting that sensitivity of O_3 forma-

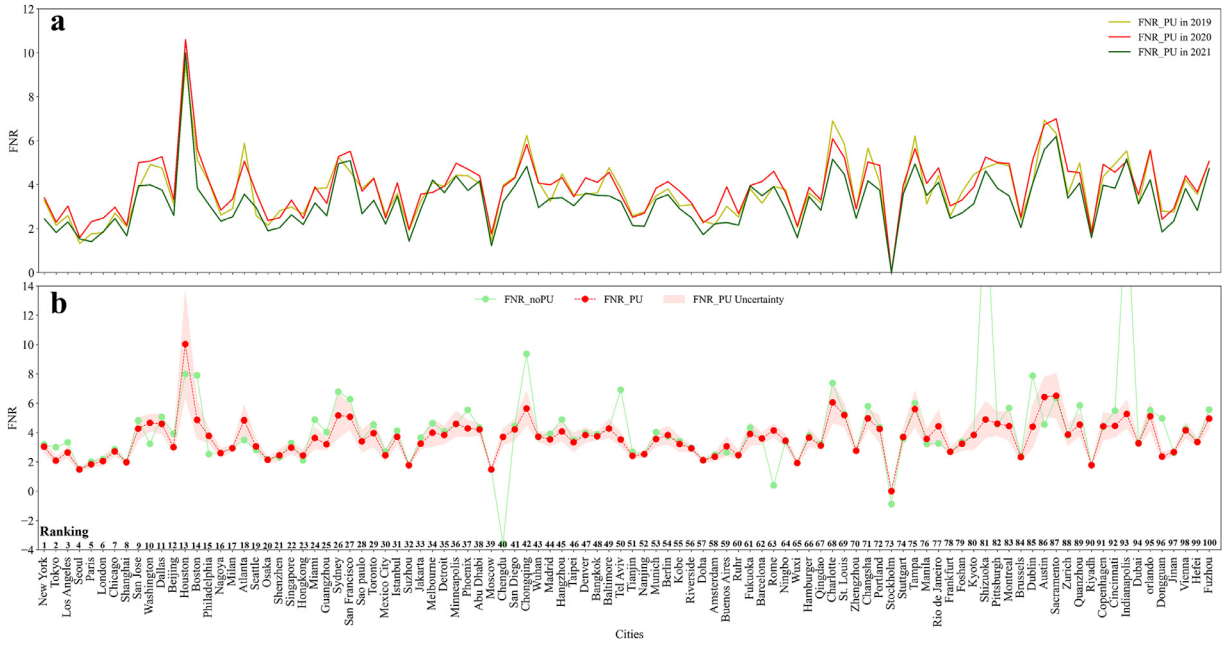

Fig. 8 – (a) Annual and (b) three-year mean FNR ($HCHO/NO_2$) of the top 100 cities ranked by global GDP from 2019 to 2021

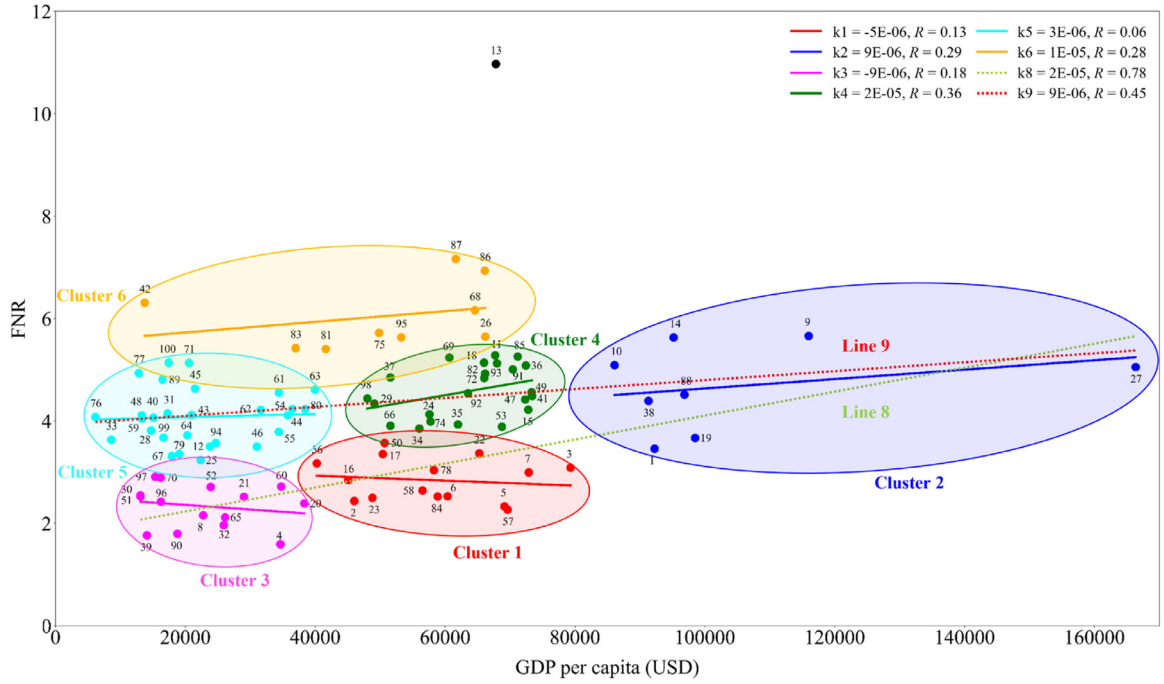

Fig. 9 – Clustering of GDP and FNR ($HCHO/NO_2$) of the top 100 cities worldwide (Ranking number is shown in Fig. 8 and the city location is shown in Appendix A Fig. S1)

tion continue to shift towards to NO_x-limited regimes, and the urban O_3 content was more sensitive to the variation of NO_x, which showed little relationship with the degree of economic development.

The cities in Cluster 3 are in the lower FNR region, and have lower per capita GDP, the FNR of cities with different economic levels does not change much, their O_3 sensitivity regimes are roughly similar. FNR had a downward trend with the increase of per capita GDP, indicating that with the increase of urban economy, the sensitivity of O_3 formation is more dependent on the VOC-limited regimes, O_3 formation is more sensitive to the variation of VOCs, which has little relationship with the degree of economic development. The cities in cluster 2 hold the highest per capita GDP and their FNR show an upward trend with economic development, indicating that the O_3 formation in these cities is more sensitive to NO_x emis-

sion, the cities in cluster 1 and cluster 4 present equivalent level of per capita GDP, while their FNR shows opposite trends with economic growth, their FNR shows opposite trends with economic growth, indicating that these cities are currently in a transitional regime of O_3 sensitivity. It is important to note that Houston exhibits an unusually high FNR and is a typical city for us to explore next, and we will figure out the reasons for Houston's high FNR and make the regimes of Houston's ozone sensitivity clear, although it looks like NO_x-limited regimes at present.

3. Conclusions

We have used the formaldehyde and NO_2 observations of TROPOMI satellite to examine the impact of the global reduction of human production activities level caused by the COVID-19 pandemic on O_3 sensitivity. Unlike previous researches, we aim to depict the evolution orientation of O_3 sensitivity, without focusing on the determination of FNR threshold, which have no unified numbers yet. We used a relative uncertainty threshold to weed out noisy data, which makes data analysis and processing smoother. Our satellite FNR presents a good correlation with EPA FNR and can be used to characterize ozone sensitivity regimes at the global scale. We found that the outbreak of the COVID-19 pandemic did not change the pattern of global ozone sensitivity, but during this period, the global ozone sensitivity regimes was transforming or strengthening to VOC-limited regimes due to the significant decline of human production activities levels. During the COVID-19 pandemic, ozone sensitivity in Eastern China and East Africa continued to shift to VOC-limited regimes, while India, Western Europe and North America first moved to NO_x-limited regimes, and then changed to VOC-limited regimes with the resumption of production and the increase in travel. There is a close relationship between economic development and the evolution of ozone sensitivity. According to the clustering, we found that urban ozone sensitivity tends to shift towards NO_x-limited regimes with the increase of economy. As economic growth, O_3 formation in cities with lower FNR and per capita GDP are more sensitive to changes in VOCs, while cities with higher FNR and per capita GDP are more sensitive to variations in NO_x. Cities with intermediate FNR and GDP are good evidence of the existence of transitional regimes. Our study highlights the importance of using TROPOMI satellite observations to discover variations in ozone production sensitivity, and identifies the driving role of urban economic development in orienting the evolution of ozone sensitivity regimes.

Declaration of competing interest

The authors declare that they have no known competing financial interests or personal relationships that could have appeared to influence the work reported in this article.

CRediT authorship contribution statement

Dakang Wang: Writing – review & editing, Writing – original draft, Resources, Methodology, Conceptualization. **Dongchuan Pu:** Writing – review & editing, Visualization, Resources, Methodology, Formal analysis, Data curation. **Isabelle De Smedt:** Writing – original draft, Validation, Methodology, Data curation, Conceptualization. **Lei Zhu:** Validation, Supervision, Methodology, Funding acquisition, Formal analysis, Conceptualization. **Xiankun Yang:** Visualization, Resources, Methodology, Investigation, Formal analysis, Conceptualization. **Wenfu Sun:** Methodology, Investigation, Formal analysis. **Hui Xia:** Visualization, Validation, Data curation. **Zhaolong Song:** Visualization, Investigation, Data curation. **Xicheng Li:** Methodology, Data curation, Conceptualization. **Juan Li:** Visualization, Software, Methodology. **Aoxing Zhang:** Validation, Software, Methodology, Conceptualization. **Xu Feng:** Writing – original draft, Methodology, Investigation, Conceptualization. **Yuyang Chen:** Software, Data curation. **Xin Yang:** Writing – review & editing, Methodology, Formal analysis, Conceptualization. **Tzung-May Fu:** Writing – review & editing, Supervision, Methodology, Conceptualization. **Jinnian Wang:** Writing – review & editing, Supervision, Methodology, Conceptualization.

Acknowledgments

This work was supported by the National Key R&D Program (No. 2021YFE0117300), the National Natural Science Foundation of China (No. 42375090), Shenzhen Key Laboratory of Precision Measurement and Early Warning Technology for Urban Environmental Health Risks (No. ZDSYS20220606100604008), Guangdong Basic and Applied Basic Research Foundation (No. 2021A1515110713), Guangdong University Research Project Science Team (No. 2021KCXTD004), the Major Talent Project of Guangdong Province (No. 2021QN020924), Shandong Provincial Natural Science Foundation, China (No. ZR2020QD012) and Shenzhen Science and Technology Program (Nos. KQTD20210811090048025, JCYJ20210324104604012 and JCYJ20220530115404009). This work was also supported by the Center for Computational Science and Engineering at Southern University of Science and Technology.

Appendix A Supplementary data

Supplementary material associated with this article can be found in the online version at doi:10.1016/j.jes.2024.07.029.

References

Acdan, J.J.M., Pierce, R.B., Dickens, A.F., Adelman, Z., Nergui, T., 2023. Examining TROPOMI formaldehyde to nitrogen dioxide ratios in the Lake Michigan region: implications for ozone exceedances. Atmos. Chem. Phys. 23 (14), 7867–7885.

Bauwens, M., Compernolle, S., Stavrakou, T., Müller, J.F., van Gent, J., Eskes, H., et al., 2020. Impact of Coronavirus outbreak on NO_2 pollution assessed using TROPOMI and OMI Observations. Geophys. Res. Lett. 47 (11), e2020GL087978.

Campbell, P., Zhang, Y., Yahya, K., Wang, K., Hogrefe, C., Pouliot, G., et al., 2015. A multi-model assessment for the 2006 and 2010 simulations under the air quality model evaluation international initiative (AQMEII) phase 2 over North America: Part I. Indicators of the sensitivity of O_3 and $PM_{2.5}$ formation regimes. Atmos. Environ. 115, 569–586.

Campbell, P.C., Tong, D., Tang, Y., Baker, B., Lee, P., Saylor, R., et al., 2021. Impacts of the COVID-19 economic slowdown on ozone pollution in the U.S. Atmos. Environ. 264, 118713.

Chan, K.L., Wiegner, M., van Geffen, J., De Smedt, I., Alberti, C., Cheng, Z., et al., 2020. MAX-DOAS measurements of tropospheric NO_2 and HCHO in Munich and the comparison to OMI and TROPOMI satellite observations. Atmos. Meas. Tech. 13 (8), 4499–4520.

Cooper, M.J., Martin, R.V., Hammer, M.S., Levelt, P.F., Veefkind, P., Lamsal, L.N., et al., 2022. Global fine-scale changes in ambient NO_2 during COVID-19 lockdowns. Nature 601 (7893), 380–387.

Crowder, S., Delker, C., Forrest, E., Martin, N., 2020. Monte Carlo methods for the propagation of uncertainties. In: S. Crowder, et al., Eds.), Introduction to Statistics in Metrology. Springer International Publishing, Cham, pp. 153-180.

De Smedt, I., Pinardi, G., Vigouroux, C., Compernolle, S., Bais, A., Benavent, N., et al., 2021. Comparative assessment of TROPOMI and OMI formaldehyde observations and validation against MAX-DOAS network column measurements. Atmos. Chem. Phys. 21 (16), 12561–12593.

Dienhart, D., Crowley, J.N., Bourtsoukidis, E., Edtbauer, A., Eger, P.G., Ernle, L., et al., 2021. Measurement report: Observation-based formaldehyde production rates and their relation to OH reactivity around the Arabian Peninsula. Atmos. Chem. Phys. 21 (23), 17373–17388.

Dunker, A.M., Wilson, G., Bates, J.T., Yarwood, G., 2020. Chemical sensitivity analysis and uncertainty analysis of ozone production in the comprehensive air quality model with extensions applied to Eastern Texas. Environ. Sci. Technol. 54 (9), 5391–5399.

Facciolà, A., Laganà, P., Caruso, G., 2021. The COVID-19 pandemic and its implications on the environment. Environ. Res. 201, 111648.

Hong, Q., Liu, C., Hu, Q., Zhang, Y., Xing, C., Su, W., et al., 2021. Evaluating the feasibility of formaldehyde derived from hyperspectral remote sensing as a proxy for volatile organic compounds. Atmos. Res. 264, 105777.

Huang, C., Ju, T., Geng, T., Fan, J., Peng, S., Xia, X., et al., 2023. Spatial and temporal distribution of HCHO and its pollution sources based on satellite remote sensing: a case study of the Yangtze River economic Belt. Environ. Res. Commun. 5 (7), 075014.

Jeon, W., Choi, Y., Souri, A.H., Roy, A., Diao, L., Pan, S., et al., 2018. Identification of chemical fingerprints in long-range transport of burning induced upper tropospheric ozone from Colorado to the North Atlantic Ocean. Sci. Total Environ. 613-614, 820–828.

Jin, X., Fiore, A., Boersma, K.F., Smedt, I.D., Valin, L., 2020. Inferring changes in summertime surface ozone–NO_x–VOC chemistry over U.S. Urban areas from two decades of satellite and ground-based observations. Environ. Sci. Technol. 54 (11), 6518–6529.

Jin, X., Fiore, A.M., Murray, L.T., Valin, L.C., Lamsal, L.N., Duncan, B., et al., 2017. Evaluating a space-based indicator of surface ozone-NO_x-VOC sensitivity over midlatitude source regions and application to decadal trends. J. Geophys. Res. Atmos. 122 (19), 461 10, 439-10.

Jin, X., Holloway, T., 2015. Spatial and temporal variability of ozone sensitivity over China observed from the Ozone Monitoring Instrument. J. Geophys. Res. Atmos. 120 (14), 7229–7246.

Johnson, M.S., Souri, A.H., Philip, S., Kumar, R., Naeger, A., Geddes, J., et al., 2023. Satellite remote-sensing capability to assess tropospheric-column ratios of formaldehyde and nitrogen dioxide: case study during the Long Island Sound Tropospheric Ozone Study 2018 (LISTOS 2018) field campaign. Atmos. Meas. Tech. 16 (9), 2431–2454.

Jones, M.W., Peters, G.P., Gasser, T., Andrew, R.M., Schwingshackl, C., Gütschow, J., et al., 2023. National contributions to climate change due to historical emissions of carbon dioxide, methane, and nitrous oxide since 1850. Sci. Data 10 (1), 155.

Kerr, G.H., Goldberg, D.L., Anenberg, S.C., 2021. COVID-19 pandemic reveals persistent disparities in nitrogen dioxide pollution. Proc. Natl. Acad. Sci. 118 (30), e2022409118.

Larson, N.M., 1986. Uncertainty propagation from raw data to final results. Radiation Effects 96 (1-4), 251–254.

Lee, H.-J., Chang, L.-S., Jaffe, D.A., Bak, J., Liu, X., Abad, G.G., et al., 2022. Satellite-based diagnosis and numerical verification of ozone formation regimes over nine megacities in East Asia. Remote. Sens. 14, 1285.

Li, D., Wang, S., Xue, R., Zhu, J., Zhang, S., Sun, Z., et al., 2021a. OMI-observed HCHO in Shanghai, China, during 2010–2019 and ozone sensitivity inferred by an improved HCHO / NO_2 ratio. Atmos. Chem. Phys. 21 (20), 15447–15460.

Li, K., Jacob, D.J., Liao, H., Qiu, Y., Shen, L., Zhai, S., et al., 2021b. Ozone pollution in the North China Plain spreading into the late-winter haze season. Proc. Natl. Acad. Sci. 118 (10), e2015797118.

Liu, C., Shi, K., 2021. A review on methodology in O_3-NO_x-VOC sensitivity study. Environ. Pollut. 291, 118249.

Liu, J., Li, X., Tan, Z., Wang, W., Yang, Y., Zhu, Y., et al., 2021. Assessing the ratios of formaldehyde and glyoxal to NO_2 as indicators of O_3–NO_x–VOC sensitivity. Environ. Sci. Technol. 55 (16), 10935–10945.

Martin, R.V., Fiore, A.M., Van Donkelaar, A., 2004. Space-based diagnosis of surface ozone sensitivity to anthropogenic emissions. Geophys. Res. Lett. 31 (6), 1–4.

Misra, P., Takigawa, M., Khatri, P., Dhaka, S.K., Dimri, A.P., Yamaji, K., et al., 2021. Nitrogen oxides concentration and emission change detection during COVID-19 restrictions in North India. Sci. Rep. 11 (1), 9800.

Miyazaki, K., Bowman, K.W., Sekiya, T., Takigawa, M., Neu, J.L., Sudo, K., et al., 2020. Global tropospheric ozone responses to reduced NO_x emissions linked to the COVID-19 worldwide lockdowns. Sci. Adv. 7 (24), 1–14.

Ren, B., Xie, P., Xu, J., Li, A., Qin, M., Hu, R., et al., 2022a. Vertical characteristics of NO_2 and HCHO, and the ozone formation regimes in Hefei. China. Sci. Total Environ. 823, 153425.

Ren, J., Guo, F., Xie, S., 2022b. Diagnosing ozone–NO_x–VOC sensitivity and revealing causes of ozone increases in China based on 2013–2021 satellite retrievals. Atmos. Chem. Phys. 22 (22), 15035–15047.

Savtchenko, A.K., Khayat, M.G., 2021. NO_2 anomalies - economy attribution and rapid climate response. Atmos. Environ. 254, 118351.

Schroeder, J.R., Crawford, J.H., Fried, A., Walega, J., Weinheimer, A., Wisthaler, A., et al., 2017. New insights into the column CH_2O/NO_2 ratio as an indicator of near-surface ozone sensitivity. J. Geophys. Res. Atmos. 122 (16), 8885–8907.

Seinfeld, J.H., 1989. Urban Air Pollution: State of the Science. Science 243 (4892), 745–752.

Selin, N.E., Wu, S., Nam, K.M., Reilly, J.M., Paltsev, S., Prinn, R.G., et al., 2009. Global health and economic impacts of future ozone pollution. Environ. Res. Lett. 4 (4), 044014.

Sillman, S., Samson, P.J., 1995. Impact of temperature on oxidant photochemistry in urban, polluted rural and remote environments. J. Geophys. Res. Atmos. 100 (D6), 11497–11508.

Souri, A.H., Johnson, M.S., Wolfe, G.M., Crawford, J.H., Fried, A., Wisthaler, A., et al., 2023. Characterization of errors in satellite-based HCHO/NO_2 tropospheric column ratios with respect to chemistry, column-to-PBL translation, spatial

representation, and retrieval uncertainties. Atmos. Chem. Phys. 23 (3), 1963–1986.
Souri, A.H., Nowlan, C.R., Wolfe, G.M., Lamsal, L.N., Chan Miller, C.E., Abad, G.G., et al., 2020. Revisiting the effectiveness of HCHO/NO_2 ratios for inferring ozone sensitivity to its precursors using high resolution airborne remote sensing observations in a high ozone episode during the KORUS-AQ campaign. Atmos. Environ. 224, 117341.
Stavrakou, T., Müller, J.F., Bauwens, M., Boersma, K.F., van Geffen, J., 2020. Satellite evidence for changes in the NO_2 weekly cycle over large cities. Sci. Rep. 10 (1), 10066.
Stowell, J.D., Kim, Y.-m., Gao, Y., Fu, J.S., Chang, H.H., Liu, Y., 2017. The impact of climate change and emissions control on future ozone levels: Implications for human health. Environ. Int. 108, 41–50.
Sun, K., Zhu, L., Cady-Pereira, K., Chan Miller, C., Chance, K., Clarisse, L., et al., 2018. A physics-based approach to oversample multi-satellite, multispecies observations to a common grid. Atmos. Meas. Tech. 11 (12), 6679–6701.
Sun, W., Zhu, L., De Smedt, I., Bai, B., Pu, D., Chen, Y., et al., 2021a. Global significant changes in formaldehyde (HCHO) columns observed from space at the early stage of the COVID-19 pandemic. Geophys. Res. Lett. 48 (4), 2e020GL091265.
Sun, Y., Yin, H., Liu, C., Zhang, L., Cheng, Y., Palm, M., et al., 2021b. Mapping the drivers of formaldehyde (HCHO) variability from 2015 to 2019 over eastern China: insights from Fourier transform infrared observation and GEOS-Chem model simulation. Atmos. Chem. Phys. 21 (8), 6365–6387.
van Geffen, J., Eskes, H., Compernolle, S., Pinardi, G., Verhoelst, T., Lambert, J.C., et al., 2022. Sentinel-5P TROPOMI NO_2 retrieval: impact of version v2.2 improvements and comparisons with OMI and ground-based data. Atmos. Meas. Tech. 15 (7), 2037–2060.
Vazquez Santiago, J., Jaimes Palomera, M., Resendiz Martinez, C., Hernandez Matamoros, A., Hata, H., Inoue, K., et al., 2024. Ozone responses to reduced precursor emissions: a modeling analysis on how attainable goals can improve air quality in the Mexico City Metropolitan Area. Sci. Total Environ. 912, 169180.
Verhoelst, T., Compernolle, S., Pinardi, G., Lambert, J.C., Eskes, H.J., Eichmann, K.U., et al., 2021. Ground-based validation of the Copernicus Sentinel-5P TROPOMI NO_2 measurements with the NDACC ZSL-DOAS, MAX-DOAS and Pandonia global networks. Atmos. Meas. Tech. 14 (1), 481–510.
Verstraeten, W.W., Neu, J.L., Williams, J.E., Bowman, K.W., Worden, J.R., Boersma, K.F., 2015. Rapid increases in tropospheric ozone production and export from China. Nat. Geosci. 8 (9), 690–695.
Vigouroux, C., Langerock, B., Bauer Aquino, C.A., Blumenstock, T., Cheng, Z., De Mazière, M., et al., 2020. TROPOMI–Sentinel-5 Precursor formaldehyde validation using an extensive network of ground-based Fourier-transform infrared stations. Atmos. Meas. Tech. 13 (7), 3751–3767.
Wang, H., Huang, C., Tao, W., Gao, Y., Wang, S., Jing, S., et al., 2022. Seasonality and reduced nitric oxide titration dominated ozone increase during COVID-19 lockdown in eastern China. npj Clim. Atmos. Sci. 5 (1), 24.
Wang, Q., Li, L., 2021. The effects of population aging, life expectancy, unemployment rate, population density, per capita GDP, urbanization on per capita carbon emissions. Sustain. Prod. Consump. 28, 760–774.
Xue, J., Zhao, T., Luo, Y., Miao, C., Su, P., Liu, F., et al., 2022. Identification of ozone sensitivity for NO_2 and secondary HCHO based on MAX-DOAS measurements in northeast China. Environ. Int. 160, 107048.
Yen, Y.-C., Ku, C.-H., Hsiao, T.-C., Chi, K.H., Peng, C.-Y., Chen, Y.-C., 2023. Impacts of COVID-19's restriction measures on personal exposure to VOCs and aldehydes in Taipei City. Sci. Total Environ. 880, 163275.
Zhan, J., Ma, W., Song, B., Wang, Z., Bao, X., Xie, H.-B., et al., 2023. The contribution of industrial emissions to ozone pollution: identified using ozone formation path tracing approach. npj Clim. Atmos. Sci. 6 (1), 37.
Zhu, L., Jacob, D.J., Keutsch, F.N., Mickley, L.J., Scheffe, R., Strum, M., et al., 2017. Formaldehyde (HCHO) as a hazardous air pollutant: mapping surface air concentrations from satellite and inferring cancer risks in the United States. Environ. Sci. Technol. 51 (10), 5650–5657.
Zhu, L., Jacob, D.J., Mickley, L.J., Marais, E.A., Cohan, D.S., Yoshida, Y., et al., 2014. Anthropogenic emissions of highly reactive volatile organic compounds in eastern Texas inferred from oversampling of satellite (OMI) measurements of HCHO columns. Environ. Res. Lett. 9 (11), 114004.